Journal of Alloys and Compounds 509 (2011) 6043–6048

Contents lists available at ScienceDirect

Journal of Alloys and Compounds

journal homepage: www.elsevier.com/locate/jallcom

Microstructure and room temperature properties of a high-entropy TaNbHfZrTi alloy

O.N. Senkov[a,b,*], J.M. Scott[a,b], S.V. Senkova[a,b], D.B. Miracle[a], C.F. Woodward[a]

[a] Air Force Research Laboratory, Materials and Manufacturing Directorate, Wright-Patterson Air Force Base, Dayton, OH 45433, USA
[b] UES, Inc., Dayton, OH 45432, USA

ARTICLE INFO

Article history:
Received 23 December 2010
Received in revised form 25 February 2011
Accepted 28 February 2011
Available online 8 March 2011

Keywords:
Alloy design
Crystallography
Microstructure
Mechanical properties

ABSTRACT

A new refractory alloy, $Ta_{20}Nb_{20}Hf_{20}Zr_{20}Ti_{20}$, produced by vacuum arc-melting followed by hot isostatic pressing (HIPing) at $T = 1473$ K and $P = 207$ MPa for 3 h has predominantly a single-phase body-centered cubic (BCC) structure with the lattice parameter $a = 340.4$ pm. The alloy density and Vickers microhardness are $\rho = 9.94$ g/cm^3 and $H_v = 3826$ MPa. The alloy has high compression yield strength ($\sigma_{0.2} = 929$ MPa) and ductility ($\varepsilon > 50\%$). The alloy shows considerable strain hardening and homogeneous deformation. A simple model of solid-solution strengthening is proposed to explain the behavior.

1. Introduction

Metallic alloys with superior mechanical and functional properties remain in high demand for the aerospace industry. A new strategy for achieving stable, multi-component, high-temperature alloys has recently been proposed [1–3]. In these so-called high entropy alloys (HEAs) the configurational entropy of a multi-component solid solution phase is maximized so that the entropy of mixing stabilizes disordered solid solution phases relative to possible intermetallic phases. In order to achieve high entropy of mixing, the alloy must have typically five or more major elements of roughly equi-molar concentrations. This concept has shown merit with the production of several experimental alloy compositions with face center cubic (FCC) and/or body center cubic (BCC) crystal structures and favorable combinations of strength and ductility [1,4–11]. Almost all HEAs for which mechanical properties have been reported are based on a CoCrFeNi composition to which additional elements such as Al [1,2,4,12–14], Cu [1,2,6], Si [15], Mn [4], Mo [11], and/or Ti [5,6,8] have been added. These HEAs exhibit very high room temperature compression strength, often exceeding 1500 MPa. The room temperature compression strain of these alloys in cast condition generally does not exceed 5–7%; however, few HEAs show compression strains as high as 25–33% [5–9,16]. Annealing has been found to improve ductility of cast HEAs [9,16]. Similar to conventional alloys, a rapid decrease in strength of HEAs occurs at temperatures above $\sim 0.6T_m$, where T_m is the melting temperature, and at $T = 1273$K the strength of CoCrFeNi-based HEAs approaches $\sim$100 MPa [1,17].

Two refractory HEAs, $Ta_{25}Nb_{25}W_{25}Mo_{25}$ and $Ta_{20}Nb_{20}W_{20}Mo_{20}V_{20}$, with considerably increased T_m and thus improved high-temperature strength values, have been reported recently [18,19]. These alloys have a single-phase BCC structure and high Vickers hardness of 4.5 GPa and 5.3 GPa, respectively, and they produced a very high yield strength ($\sigma_{0.2}$) in the temperature range from 296 K to 1873 K. For example, $\sigma_{0.2}$ of 405 MPa and 477 MPa at 1873 K were reported for the $Ta_{25}Nb_{25}W_{25}Mo_{25}$ and $Ta_{20}Nb_{20}W_{20}Mo_{20}V_{20}$ alloys, respectively. Unfortunately, these refractory alloys have a high density and exhibited low ductility at room temperature (RT). Moreover, presence of V accelerated oxidation of the $Ta_{20}Nb_{20}W_{20}Mo_{20}V_{20}$ alloy at high temperatures [20]. In this paper, we report results on development and characterization of a new refractory HEA, $Ta_{20}Nb_{20}Hf_{20}Zr_{20}Ti_{20}$ with an estimated $T_m = 2522$ K. Replacement of heavier W, Mo and V with lighter elements such as Hf, Zr and Ti was found to considerably decrease the alloy density and improve RT ductility.

2. Experimental procedures

The Ta–Nb–Hf–Zr–Ti alloy was prepared by vacuum arc melting of the equimolar mixtures of the corresponding elements. Ti, Zr and Hf were in the form of 3.2 mm diameter slugs with a purity of 99.98%, 99.95% and 99.9%, respectively. Niobium and tantalum were in the form of 1.0 and 2.0 mm wires, and their purities were 99.95% and 99.9%, respectively. Arc melting of the alloy was conducted on a water-cooled copper plate. To achieve homogeneous distribution of elements in the alloy, it was

* Corresponding author at: UES, Inc. 4401 Dayton-Xenia Rd., Dayton, OH 45432, USA. Tel.: +1 937 2551320; fax: +1 937 656 7292.
E-mail address: oleg.senkov@wpafb.af.mil (O.N. Senkov).

0925-8388/$ – see front matter © 2011 Elsevier B.V. All rights reserved.
doi:10.1016/j.jallcom.2011.02.171

Table 1
Chemical composition of the TaNbHfZrTi alloy produced by vacuum arc melting.

Composition	Ta	Nb	Hf	Zr	Ti
at.%	19.68	18.93	20.46	21.23	19.7
wt.%	30.04	14.84	30.82	16.34	7.96

re-melted three times, was flipped for each melt, and was in a liquid state for about 5 min during each melting event. The prepared button was about 8 mm thick and had shiny surfaces. The actual alloy composition is given in Table 1. To close porosity presented in the as-solidified sample, it was hot isostatically pressed (HIP) at 1473 K, 207 MPa for 3 h. Prior to HIPing, the sample was wrapped with a 0.1 mm thick Ta foil, placed in a low carbon 1010 steel container with the wall thickness of 0.89 mm, and the container was vacuum sealed.

The crystal structure was identified with the use of a Rigaku X-ray diffractometer, Cu Kα radiation, and the 2θ range of 5–140°. The density of the alloy was measured with an AccuPyc 1330 V1.03 pycnometer. Vickers microhardness was measured on polished cross-section surfaces using a 136° Vickers diamond pyramid under 0.5 kg load applied for 30 s. The microstructure was analyzed with the use of a scanning electron microscope (SEM) equipped with the backscatter electron (BSE) detector.

Cylindrical specimens for compression testing were 3.7 mm in diameter and ~5.6 mm in height. The specimen axis was perpendicular to the button surface, which was in contact with the copper plate during arc melting. Compression tests to a 50% height reduction were conducted at RT using a computer-controlled Instron (Instron, Norwood, MA) mechanical testing machine outfitted with silicon carbide dies. A thin Teflon foil was used between the compression faces and silicon carbide dies to reduce friction. The deformation of the samples was video-recorded and the strain measured using optical techniques. A constant ramp speed of 0.0056 mm/s was applied to the samples, which corresponds to an initial strain rate of 0.001 s^{-1}.

3. Results

Fig. 1 shows the X-ray diffraction pattern of the cast and HIP'd alloy. All seven major diffraction peaks on this X-ray pattern have been identified as belonging to a body centered cubic (BCC) phase. The indexes of the crystal planes corresponding to the X-ray diffraction peaks are indicated in Fig. 1. The lattice parameter of the BCC phase was determined to be $a = 340.4 \pm 0.1$ pm, both in the as-cast and HIP conditions. A small peak at $2\theta = 24.9°$ indicates the presence of a minor, likely hexagonal, phase. The density of the alloy after HIPing was determined to be $\rho_1 = 9.94 \pm 0.01$ g/cm^3. Vickers microhardness H_v of the alloy was measured in sixteen randomly selected locations and the average value was 3826 MPa. The scatter around the average microhardness value was $\Delta H_v = \pm 80$ MPa.

The RT engineering stress, σ, vs. engineering strain, ε curve of the $Ta_{20}Nb_{20}Hf_{20}Zr_{20}Ti_{20}$ alloy obtained during compression testing is given in Fig. 2. The yield strength, $\sigma_{0.2}$, was 929 ± 15 MPa. After yielding, the alloy showed continuous strengthening at a nearly constant rate, $\gamma = d\sigma/d\varepsilon = 3360$ MPa. The alloy was deformed to 50% compression strain without any evidence of fracture. The deformation curves of $Ta_{20}Nb_{20}W_{20}Mo_{20}V_{20}$ and $Ta_{25}Nb_{25}W_{25}Mo_{25}$ alloys [19], which have $\sigma_{0.2} = 1246$ MPa and 1058 MPa, respectively, but much lower ductility, are also shown in Fig. 2 for comparison. Due to high strain hardening, preliminary 10% compression strain of the new $Ta_{20}Nb_{20}Hf_{20}Zr_{20}Ti_{20}$ alloy would allow achieving the yield strength of 1330 MPa and still retain good ductility, thus providing the mechanical properties that are much superior to the previously reported refractory HEAs.

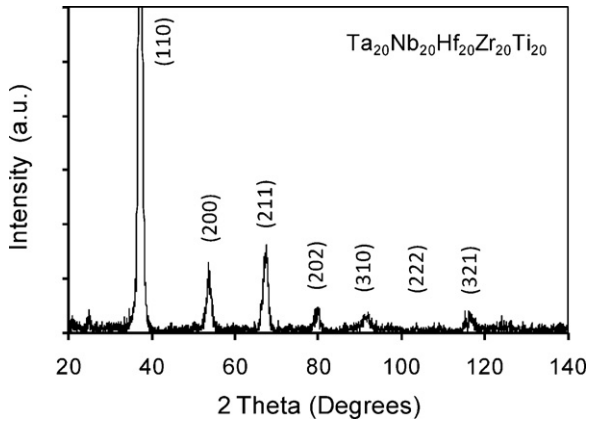

Fig. 1. X-ray diffraction pattern of the TaNbHfZrTi alloy. The indexed peaks belong to a BCC crystal lattice with the lattice parameter $a = 340.4$ pm.

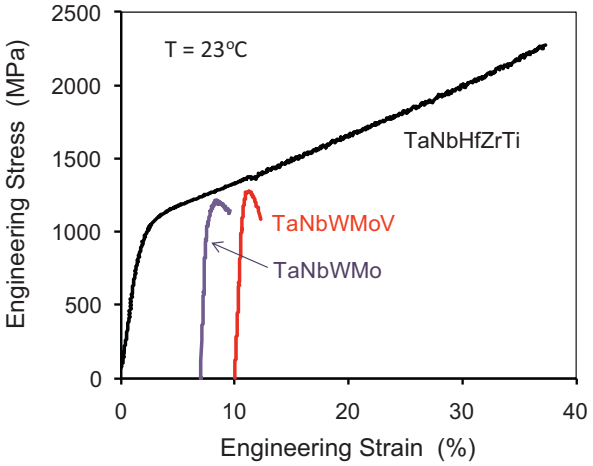

Fig. 2. Engineering stress vs. engineering strain compression curves of the $Ta_{20}Nb_{20}Hf_{20}Zr_{20}Ti_{20}$ alloy (present work) and $Ta_{20}Nb_{20}W_{20}Mo_{20}V_{20}$ and $Ta_{25}Nb_{25}W_{25}Mo_{25}$ alloys (from ref. [13]).

The microstructure of the HIP'd $Ta_{20}Nb_{20}Hf_{20}Zr_{20}Ti_{20}$ alloy consisted of equiaxial dendritic grains of about 100–200 μm (Fig. 3a). A rather uniform deformation, with a very small sample barreling and no evidence of strain localization, occurred at RT (Fig. 3b). Deformed grains that were elongated in the radial direction and the dendrite alignment in the same direction were clearly seen (Fig. 3c). Images at higher magnification revealed deformation twins and cracking along some grain boundaries in the deformed sample (Fig. 3d).

4. Discussion

In spite of heavy alloying, the $Ta_{20}Nb_{20}Hf_{20}Zr_{20}Ti_{20}$ alloy has predominantly a single-phase BCC crystal structure, which remains stable after HIPing at 1473 K. The absence of extra-peaks from element ordering suggests random distribution of the elements in this BCC phase. It is necessary to point out that all five elements in the alloy have the BCC crystal lattices just below their melting temperatures and no intermetallic phases are present in binary systems of these elements [21]. Ta and Nb maintain a BCC structure down to RT, and the RT lattice parameters for these elements [22] are given in Table 2. The Ta–Nb binary system is a continuous solid solution within the entire composition range. Three other elements, Hf, Zr and Ti, also form continuous solid solutions with each other, but they exhibit polymorphic transformations and have a hexagonal close packed (HCP) crystal structure at RT. Reported BCC lattice parameters for these elements, $a_{Hf} = 361.5$ pm, $a_{Zr} = 360.9$ pm and $a_{Ti} = 330.65$ pm were determined at temperatures 2016 K, 1140 K and 1155 K, respectively [21]. These values can however be extrapolated to RT by using reported coefficients of thermal expansion (CTE) for BCC Hf (9×10^{-6} K^{-1}), Zr (9×10^{-6} K^{-1}) and Ti (10.9×10^{-6} K^{-1}) [23]. Thus calculated RT BCC lattice parameters for these three elements are also given in Table 2.

Alloying of Hf, Zr and Ti with Ta and/or Nb is known to stabilize the high-temperature BCC phase and may result in a mixture of the BCC and HCP solid solution phases (or even a single BCC

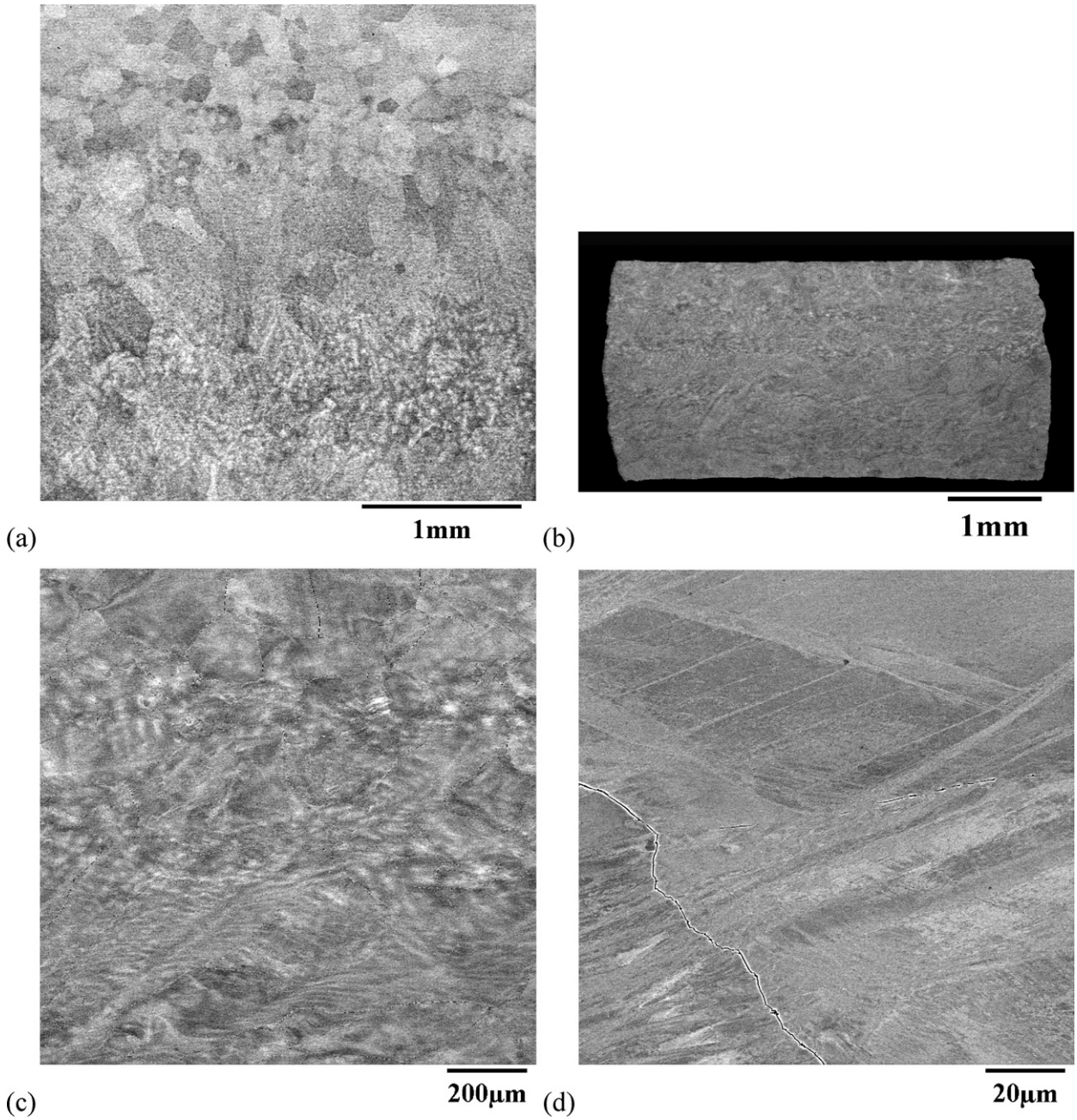

Fig. 3. SEM backscatter electron images of a longitudinal cross-section of the HIP'd $Ta_{20}Nb_{20}Hf_{20}Zr_{20}Ti_{20}$ alloy (a) before and (b, c and d) after compression deformation at room temperature.

phase in the Ti alloys) at RT. Therefore, the presence of the disordered BCC phase in the quinternary alloy, which contains 40 at.% of the BCC-stabilized elements, is expected. It is however not yet known if the BCC phase is thermodynamically stable at RT or it is metastable and formation of the low temperature HCP phase is kinetically restricted due to slow diffusivity of elements in the multicomponent alloys [1,3,24]. In order to address this question, an additional study involving long-time annealing at temperatures below 600 °C is required.

Using rule of mixtures (i.e. Vegard's law [25]), one can calculate the 'theoretical' crystal lattice parameter a_{mix} of the disordered BCC solid solution:

$$a_{mix} = \sum c_i a_i \quad (1)$$

Table 2
The lattice parameter, a, of the BCC crystal structure, density, ρ, Vickers microhardness, H_v, and yield strength, $\sigma_{0.2}$, of the pure metals and the studied alloy.

Metal	Ta	Nb	Hf	Zr	Ti	Alloy Calc.	Alloy Exp.
a (pm)	330.3	330.1	355.9	358.2	327.6	340.9	340.4
ρ (g/cm^3)	16.65	8.57	13.31	6.51	4.51	9.89	9.94
H_v (MPa)	873	1320	1760	903	970	1165	3826
$\sigma_{0.2}$ (MPa)	170	240	240	280	195	226	929

Here c_i is the atomic fraction of element i. The calculated (Calc.) a_{mix} is given in Table 2. The experimental (Exp) a value, determined from the X-ray diffraction pattern, is also given in this table. It can be seen that the calculated and experimental values of a are practically the same, which indicates that the lattice parameter of the alloy follows rule of mixtures. This analysis supports the X-ray results that the alloying elements are randomly distributed in the BCC phase.

The theoretical density, ρ_{mix}, of a disordered solid solution is given by Eq. (2):

$$\rho_{mix} = \frac{\sum c_i A_i}{\sum c_i A_i / \rho_i} \quad (2)$$

where A_i and ρ_i are the atomic weight and density of element i. The ρ_i values of the alloying elements taken from ref. [26] and the calculated ρ_{mix} value of the alloy (9.89 g/cm^3) are given in Table 2. It can be seen that the calculated density is about 0.50% smaller than the experimentally determined density of the alloy (9.94 g/cm^3). This very small difference can be due to experimental errors in determining the alloy composition and density. We may thus conclude that the alloy density follows the rule of mixtures, which is also in agreement with the random (disordered) distribution of the alloying elements in the BCC lattice of the alloy.

The RT yield strength and Vickers microhardness of the HIP'd $Ta_{20}Nb_{20}Hf_{20}Zr_{20}Ti_{20}$ alloy are $\sigma_{0.2}$ = 929 MPa and H_v = 3826 MPa, which gives the hardness to stress ratio $\phi = H_v/\sigma_{0.2}$ = 4.12. This is noticeably higher than the value ϕ = 3, which was predicted theoretically and observed experimentally for non-strain hardening materials [27]. Taber [27, p. 175] has noticed that ϕ = 3 also holds for pure metals and commercial alloys, regardless of the initial state of strain hardening, if the engineering stress σ_8 corresponding to the engineering strain $\varepsilon \sim 8\%$, which is the average plastic strain during Vickers indentation, is used instead of $\sigma_{0.2}$. From the deformation behavior of the $Ta_{20}Nb_{20}Hf_{20}Zr_{20}Ti_{20}$ alloy (see Fig. 2), σ_8 = 1270 MPa is obtained. This indeed gives the value $\phi = H_v/\sigma_8$ = 3.0. One may therefore conclude that the high hardness to yield strength ratio observed for the studied alloy is caused by strain hardening of the initially annealed alloy during indentation. This analysis also indicates that preliminary 8% compression straining of this alloy would allow achieving the yield strength of 1270 MPa and still retain good ductility, thus providing the mechanical properties that are much superior to previously reported HEAs. It is worth noting that, among all other high entropy alloys with the BCC structure produced so far, the $Ta_{20}Nb_{20}Hf_{20}Zr_{20}Ti_{20}$ alloy has the highest RT compression ductility (>50%) [5,8].

The microhardness and the yield strength of the $Ta_{20}Nb_{20}Hf_{20}Zr_{20}Ti_{20}$ alloy do not follow the rule of mixtures of the respective properties of the constituent elements. Indeed, Table 2 shows typical H_v [28] and $\sigma_{0.2}$ [29] values for pure elements at RT. The rule of mixtures microhardness, $(H_v)_{mix} = \sum c_i H_{vi}$, and yield strength, $(\sigma_{0.2})_{mix} = \sum c_i \sigma_{0.2i}$, of the alloy are much smaller than the respective experimental (Exp.) H_v and $\sigma_{0.2}$ values (see Table 2). The high microhardness and yield strength of the alloy are likely originated from solid solution-like strengthening.

It is widely accepted that the solid solution strengthening of metallic solid solutions arises from the elastic interactions between the local stress fields of solute atoms and those of dislocations [30–34]. The magnitude of the interaction force, f_m, increases with an increase in both the atomic size misfit parameter, δ_a, and the modulus misfit parameter, δ_G, of the solute and solvent atoms:

$$f_m = Gb^2\delta = Gb^2\left[\delta_G + \beta\delta_a\right] \quad (3)$$

Here $\delta_G = (1/G)dG/dc$, $\delta_a = (1/a)da/dc$, G is the shear modulus of the alloy, b is the magnitude of the Burgers vector, and β is a constant, which value depends on the type of the mobile dislocation.

Table 3
Atomic radius, $r = (\sqrt{3}/4)a$, and shear modulus, G, of pure elements.

Element/Property	Ta	Nb	Hf	Zr	Ti
r (pm)	143.0	142.9	154.1	155.1	141.8
G (GPa)	69	38	30	33	44

Generally, β is 2–4 for the screw dislocations and ≥16 for edge dislocations [30,32]. In a concentrated solid solution, the solute-induced stress increase, $\Delta\sigma$ can be expressed as a function of f_m, solute concentration, c, and dislocation line tension, E_L, [31,35]:

$$\Delta\sigma b^2 = A f_m^{4/3} c^{2/3} E_L^{-1/3} \quad (4)$$

Here A is a dimensionless material constant. Using the expression $E_L = Gb^2/2$ and combining Eqs. (3) and (4), the following equation for $\Delta\sigma$ is obtained [36]:

$$\Delta\sigma = A' G \delta^{4/3} c^{2/3} \quad (5)$$

where A' is a material-dependent dimensionless constant, which is of the order of 0.1 [31]. Unfortunately, the mechanisms of solid solution strengthening were developed for conventional solid solutions, in which the concentration of the matrix element (solvent) exceeds 60–70%, and these mechanisms may not be applicable to high-entropy alloys, where all elements are at almost the same atomic concentrations (≤20%) and multiple element interactions are expected. Nevertheless, an attempt to estimate the effects of the atomic size (lattice) and shear modulus distortions on the dislocation force, f_m, in the HEA will be given below.

Each solute in the BCC crystal lattice has 8 nearest-neighbor atoms, thus forming a 9-atom cluster. In dilute alloys with no solute interactions, the neighbors are all solvent atoms and the local lattice distortions near the solute are caused by the atomic size and modulus mismatches between the solute and the solvent atoms. In the heavily alloyed multi-component alloy, on the other hand, an i element can neighbor with different elements and the lattice distortion near this element is now a function of the atomic size and modulus mismatches between this element and all its nearest neighbors. The local environment around each element can roughly be estimated if we assume that the local concentration is equal to the average concentration of the alloy. In this case, an i element will have $Nj = 9c_j$ of j-atom neighbors and $N_i = 9c_i - 1$ of i-atom neighbors. For example, in the 5-element alloy with equimolar concentrations, an element i in the center site of the BCC unit cell will have, in average, 1.8 atoms of each of the other elements and 0.8 atoms of the same element in the corner sites. Then the lattice distortion δ_{ai} (per atom pair) in the vicinity of an element i is estimated as an average of the atomic size difference of this element with its neighbors:

$$\delta_{ai} = \frac{9}{8}\sum c_j \delta_{aij} \quad (6)$$

Here c_j is the atomic fraction of a j element in the alloy, 9 is the number of atoms in the i-centered cluster in the BCC lattice, 8 is the number of atoms neighboring with the center atom i, and $\delta_{aij} = 2(r_i - r_j)/(r_i + r_j)$ is the atomic size difference of elements i and j. Similarly, the modulus distortion, δ_{Gi}, in the vicinity of an element i is estimated as

$$\delta_{Gi} = \frac{9}{8}\sum c_j \delta_{Gij} \quad (7)$$

where $\delta_{Gij} = 2(G_i - G_j)/(G_i + G_j)$.

The atomic radii and shear moduli of the alloying elements are given in Table 3, while the calculated δ_{aij} and δ_{Gij} values are given in Table 4. Using these values and Eqs. (6) and (7), the lattice- and modulus-distortions near each element in the $Ta_{20}Nb_{20}Hf_{20}Zr_{20}Ti_{20}$ solid solution alloy were calculated and the results are given in Table 5.

Table 4
Relative atomic size difference, δ_{aij} (underlined numbers), and modulus difference, δ_{Gij} (bold numbers), of the alloying element pairs.

Element i/j $\underline{\delta_{aij}}/\boldsymbol{\delta_{Gij}}$	Ta	Nb	Hf	Zr	Ti
Ta	0	**0.58**	**0.79**	**0.71**	**0.44**
Nb	<u>0.00</u>	0	**0.24**	**0.14**	**−0.15**
Hf	<u>0.07</u>	<u>0.08</u>	0	**−0.10**	**−0.38**
Zr	<u>0.08</u>	<u>0.08</u>	<u>0.01</u>	0	**−0.29**
Ti	<u>−0.01</u>	<u>−0.01</u>	<u>−0.08</u>	<u>−0.09</u>	0

The data in Table 4 shows that the pairs of Hf and Zr elements, as well as the pairs of Ta, Nb and Ti elements have very little atomic size difference, $\delta_{aij} \approx 0.01$. On the other hand, the size difference of Hf and Zr with three other elements is about one order of magnitude higher ($\delta_{aij} \approx 0.08$). The absolute values of the estimated lattice distortions near each element (see Table 5) are of the same order ($|\delta_{ai}| \sim 0.04$–0.06). As it is expected, smaller elements, Ta, Nb and Ti, produce almost the same local tension strains ($\delta_{ai} \sim -0.04$), while larger elements, Hf and Zr, produce local compression strains ($\delta_{ai} \sim 0.05$). To roughly estimate the contribution of the lattice distortions to f_m and $\Delta\sigma$, we may consider the alloy as a pseudo-binary solid solution, with Ta, Nb and Ti as the solvents and 40 at.% of Hf plus Zr as the solutes. Designating the average strain field around Ta, Nb and Ti to be zero, the lattice distortions near Hf and Zr atoms are estimated to be $\delta_a \sim 0.09$. By assigning $G = 40$ GPa, $b = 295$ pm, $\beta = 2$, ignoring for now the modulus distortion contribution and using Eqs. (3) and (5), one can estimate $f_{ma} \approx 6.3 \times 10^{-10}$ N and $\Delta\sigma_a \approx 221$ MPa. Here subscript 'a' indicates the lattice distortion contribution.

The elastic modulus difference of the alloying elements has a wide spectrum of values, from $\delta_{Gij} = 0.10$ for the Hf–Zr atom pair to 0.79 for Ta–Hf atom pair (Table 4). Pairing of Ta atoms with other elements provides the strongest shear modulus effect (δ_{Gij} values are in the range from 0.44 for Ta–Ti to 0.79 for Ta–Hf), while Hf–Zr and Nb–Zr pairs resulted in smaller δ_{Gij} values of 0.10 and 0.14, respectively. The calculated modulus distortions near a particular element in the BCC lattice of the alloy, δ_{Gi}, also have the largest values of $\delta_{GTa} = 0.57$ near Ta atoms (Table 5), while δ_{Gi} values near other four elements are considerably smaller and their average is about −0.181. Noting that Ti, Zr, and Hf occupy the same column in the periodic table, a reflection of the common aspects of their electronic structure, and that the modulus of Nb is similar to that of these three elements, one can assert the modulus of 'the solvent' as a weighted average of these four elements. In essence the Ta interactions produce a far larger deviation in the local forces than all the other elements, and thus produce a large effective modulus misfit. Assuming that the modulus mismatch contributions to the interaction force f_{mG} and stress increase $\Delta\sigma_a$ is mainly due to Ta, these contributions are estimated to be $f_{mG} \approx 19.8 \times 10^{-10}$ N and $\Delta\sigma_G \approx 647$ MPa.

The estimated values for f_{ma} and f_{mG} are of about one order of magnitude higher as those reported for binary solid solutions [35]. This very rough analysis of the contributions of the atomic size and modulus difference to the yield strength of the alloy predicts $\sigma_{0.2} = (\sigma_{0.2})_{\text{mix}} + \Delta\sigma_a + \Delta\sigma_G \approx 1094$ MPa, which is about 18% higher than the experimentally observed $\sigma_{0.2} = 929$ MPa. This can be considered as a good agreement. Indeed, the model does not take into account thermally activated processes, which should ease the deformation processes and reduce the stress. The analysis also shows that the modulus distortions are likely to be stronger obstacles for dislocation movements in this alloy than the lattice distortions. The good ductility of the alloy at RT is probably due to simultaneous dislocation and twin activity, which effectively reduce stress localization along grain boundaries. It is apparent that the grain boundaries are the weakest structural elements along which cracks eventually develop after heavy deformation in the $Ta_{20}Nb_{20}Hf_{20}Zr_{20}Ti_{20}$ alloy.

Table 5
Calculated lattice distortion, δ_{ai}, and modulus distortion, δ_{Gi}, (Eqs. (6) and (7)) near each element in the BCC lattice of the TaNbHfZrTi alloy.

Element	Ta	Nb	Hf	Zr	Ti
δ_{ai}	−0.035	−0.035	0.049	0.057	−0.044
δ_{Gi}	0.571	−0.073	−0.331	−0.228	0.089

5. Conclusions

A refractory alloy, $Ta_{20}Nb_{20}Hf_{20}Zr_{20}Ti_{20}$, produced by vacuum arc-melting, has a single-phase body-centered cubic (BCC) structure with the lattice parameter $a = 340.44$ pm. No phase changes occur after HIPing the alloy at 1473 K, 207 MPa for 3 h. The alloy density and Vickers microhardness after HIPing were $\rho = 9.94$ g/cm^3 and $H_v = 3826$ MPa. The alloy has high compression yield strength ($\sigma_{0.2} = 929$ MPa) and ductility ($\varepsilon > 50\%$). The alloy shows considerable strengthening and homogeneous deformation. The high stress is explained by solid-solution strengthening.

Acknowledgements

Discussions with Drs. D. Dimiduk, P. Martin, S. Rao and G. Wilks are recognized. This work was supported through the Air Force Office of Scientific Research (Dr. Ali Sayir, Program Manager) and through the USAF Contract No. FA8650-10-D-5226.

References

[1] J.-W. Yeh, S.-K. Chen, S.-J. Lin, J.-Y. Gan, T.-S. Chin, T.-T. Shun, C.-H. Tsau, S.-Y. Chang, Adv. Eng. Mater. 6 (5) (2004) 299–303.
[2] J.-W. Yeh, Ann. Chim.: Sci. Mater. 31 (2006) 633–648.
[3] J.-W. Yeh, Y.-L. Chen, S.-J. Lin, S.-K. Chen, Mater. Sci. Forum 560 (2007) 1–9.
[4] Y.J. Zhou, Y. Zhang, Y.L. Wang, G.L. Chen, Mater. Sci. Eng. A 454–455 (2007) 260–265.
[5] Y.J. Zhou, Y. Zhang, Y.L. Wang, G.L. Chen, Appl. Phys. Lett. 90 (2007) 1–3, 181904/.
[6] Y.J. Zhou, Y. Zhang, F.J. Wang, Y.L. Wang, G.L. Chen, J. Alloys Compd. 466 (2008) 201–204.
[7] Y.P. Wang, B.S. Li, M.X. Ren, C. Yang, H.Z. Fu, Mater. Sci. Eng. A 491 (2008) 154–158.
[8] F.J. Wang, Y. Zhang, Mater. Sci. Eng. A 496 (2008) 214–216.
[9] L.H. Wen, H.C. Kou, J.S. Li, H. Chang, X.Y. Xue, L. Zhou, Intermetallics 17 (2009) 266–269.
[10] C.W. Tsai, M.H. Tsai, J.W. Yeh, C.C. Yang, J. Alloys Compd. 490 (2010) 160–165.
[11] J.M. Zhu, H.M. Fu, H.F. Zhang, A.M. Wang, H. Li, Z.Q. Hu, Mater. Sci. Eng., A 527 (2010) 6975–6979.
[12] K.B. Zang, Z.Y. Fu, J.Y. Zhang, W.M. Wang, H. Wang, Y.C. Wang, Q.J. Zhang, J. Shi, Mater. Sci. Eng., A 508 (2009) 214–219.
[13] Y.F. Kao, T.J. Chen, S.K. Chen, J.W. Yeh, J. Alloys Compd. 488 (2009) 57–64.
[14] C. Li, J.C. Li, M. Zhao, Q. Jiang, J. Alloys Compd. 504S (2010) S515–S518.
[15] J.M. Zhu, H.M. Fu, H.F. Zhang, A.M. Wang, H. Li, Z.Q. Hu, Mater. Sci. Eng., A 527 (2010) 7210–7214.
[16] K.B. Zang, Z.Y. Fu, J.Y. Zhang, J. Shi, W.M. Wang, H. Wang, Y.C. Wang, Q.J. Zhang, J. Alloys Compd. 502 (2010) 295–299.
[17] C.J. Tong, M.R. Chen, S.K. Chen, J.W. Yeh, T.T. Shun, S.J. Lin, S.Y. Chang, Metall. Mater. Trans. A 36A (2005) 1264–1271.
[18] O.N. Senkov, G.B. Wilks, D.B. Miracle, C.P. Chuang, P.K. Liaw, Intermetallics 18 (2010) 1758–1765.
[19] O.N. Senkov, G.B. Wilks, J.M. Scott, D.B. Miracle, Intermetallics 19 (2011) 698–706.
[20] O.N. Senkov, G.B. Wilks, D.B. Miracle, Refractory High Entropy Alloys: Microstructure and Properties, Unpublished presentation, May 2010.
[21] T.B. Massalski, H. Okamoto, P.R. Subramanian, L. Kacprzak, Binary Alloy Phase Diagrams, 2nd ed., ASM International, Materials Park, OH, USA, 1990.
[22] J.S. Kasper, International Tables for X-Ray Crystallography, Kynoch Press, Birmingham, England, 1968, pp. 45-58.
[23] M. Chase, JANAF Thermochemical Tables, 3rd ed., J. Phys. Chem. Ref. Data (1985);
J.D. Cox, CODATA Key Values for Thermodynamics, Hemisphere Publ. Co., NY, 1989;
A.T. Dinsdale, SGTE data for pure elements, CALPHAD 15 (4) (1991) 317–425.
[24] M.-H. Tsai, J.-W. Yeh, J.-Y. Gan, Thin Solid Films 516 (2008) 5527–5530.
[25] L. Vegard, Zeitschrift fur Physik 5 (1921) 17–26.

[26] WebElements: http://www.webelements.com/periodicity/density.
[27] D. Taber, The Hardness of Metals, Oxford University Press, London, 1951.
[28] Hardnesses of the elements: http://en.wikipedia.org/wiki/ Hardnesses_of_the_elements_(data_page).
[29] Goodfellow, Index of Materials: http://www.goodfellow.com/E/T.html.
[30] R.L. Fleischer, Acta Metall. 11 (1963) 203–209.
[31] R. Labusch, Acta Metall. 20 (1972) 917;
R. Labusch, Phys. Status Solidi 41 (1970) 659.
[32] L.A. Gypen, A. Deruyttere, J. Mater. Sci. 12 (1977) 1028–1033.
[33] T. Suzuki, Jap. J. Appl. Phys. 20 (1981) 449–462.
[34] C. Meyers, Mechanical Behavior of Materials, Cambridge University Press, UK, 1999.
[35] H. Mughrabi (Ed.), Materials Science and Technology, vol. 6: Plastic Deformation and Fracture of Materials, VCH, Cambridge, 1993, pp. 191–250.
[36] R.J. Arsenault (Ed.), Treatise on Materials Science and Technology, vol. 6: Plastic Deformation of Materials, Academic Press, New York, 1975, pp. 1–99.